Novel algorithm of processing optical coherence tomography images for differentiation of biological tissue pathologies

Ilya V. Turchin
Ekaterina A. Sergeeva
Lev S. Dolin
Vladislav A. Kamensky
Natalia M. Shakhova
Russian Academy of Sciences
Institute of Applied Physics
603950 Ulyanov Street, 46
Nizhny Novgorod, Russia
E-mail: ilya@ufp.appl.sci-nnov.ru

Rebecca Richards-Kortum
The University of Texas at Austin
Department of Biomedical Engineering
Austin, Texas 78712

Abstract. A numerical algorithm based on a small-angle approximation of the radiative transfer equation (RTE) is developed to reconstruct scattering characteristics of biological tissues from optical coherence tomography (OCT) images. According to the algorithm, biological tissue is considered to be a layered random medium with a set of scattering parameters in each layer: total scattering coefficient, variance of a small-angle scattering phase function, and probability of backscattering, which fully describe the OCT signal behavior versus probing depth. The reconstruction of the scattering parameters is performed by their variation to fit the experimental OCT signal by the theoretical one using a time-saving genetic algorithm. The proposed reconstruction procedure is tested on model media with known scattering parameters. The possibility to estimate scattering parameters from OCT images is studied for various regimes of OCT signal decay. The developed algorithm is applied to reconstruct optical characteristics of epithelium and stroma for normal cervical tissue and its pathologies, and the potential to distinguish between the types of pathological changes in epithelial tissue by its OCT images is demonstrated.
[DOI: 10.1117/1.2137670]

Keywords: scattering; optical properties; tissue; optical coherence tomography; genetic algorithm; radiative transfer equation; inverse problem.

Paper 04209RR received Nov. 5, 2004; revised manuscript received Jun. 22, 2005; accepted for publication Jun. 23, 2005; published online Dec. 20, 2005.

1 Introduction

Optical coherence tomography (OCT), a method for imaging the internal structure of biological tissue *in vivo* with micron resolution, has been recognized as an extremely promising tool for the diagnosis of pathological changes in biological tissue.[1–7] This fact is supported by an increasing number of publications concerning the technical development of the method, as well as revealing new medical applications for OCT. The method of OCT is undergoing the procedure of evaluation in several countries, and in some it has already been certified for medical diagnostics, including endoscopic study of mucosae (esophageal mucosa, stomach mucosa, cervical mucosa, etc.).[8] Endoscopic OCT diagnostics requires utilization of compact-size probes with a diameter of about 3 mm, which restricts maximum obtainable transversal resolution up to 10 to 20 μm at probing depths of 1 to 2 mm.[3] Dynamic focusing allows us to improve resolution several times, however, it is not available yet for endoscopic applications.[9] Nevertheless, conventional OCT provides sufficient resolution to distinguish between the epithelium and stroma of mucosa of different organs. This allows for differentiation of healthy tissue from cancer on the basis of visual analysis of OCT images, since OCT images of cancer tissue show no boundary between the layers of the tissue.[3–5] However, earlier stages of neoplasia (e.g., low-grade dysplasia) are hard to distinguish, since the boundary between mucous and submucous layers is preserved, and visually the structure of OCT images is the same as of those for normal tissue. Also, one fails to differentiate some benign and malignant states of mucosa when they both produce unstructured OCT images (an example is given in Fig. 1).[6,7] In such cases, numerical analysis of OCT images can be beneficial, since it provides quantitative information about optical characteristics of biological tissue. It is known that any pathological process causes modification of tissue microstructure, which, in its turn, results in changes of optical macro parameters.[10–12] On condition that OCT is sensitive to the changes of these parameters, numerical analysis of OCT images can be useful for objective characterization of the type and stage of a pathological process.

A possibility to estimate scattering properties of tissue layers by the dependence of OCT signal on the probing depth was demonstrated in several publications.[13–16] In the majority of papers, the theoretical models of OCT signal that are employed in reconstruction algorithms use two optical param-

Address all correspondence to Ilya Turchin, Dept. of Non-linear Dynamics and Optics, Institute of Applied Physics of the RAS, Ulyanov St., 46, Nizhny Novgorod, Province 603950, Russia. Tel: +7–8312–164804. Fax: +7–8312–363792. E-mail: ilya@ufp.appl.sci-nnov.ru

1083-3668/2005/10(6)/064024/11/$22.00 © 2005 SPIE

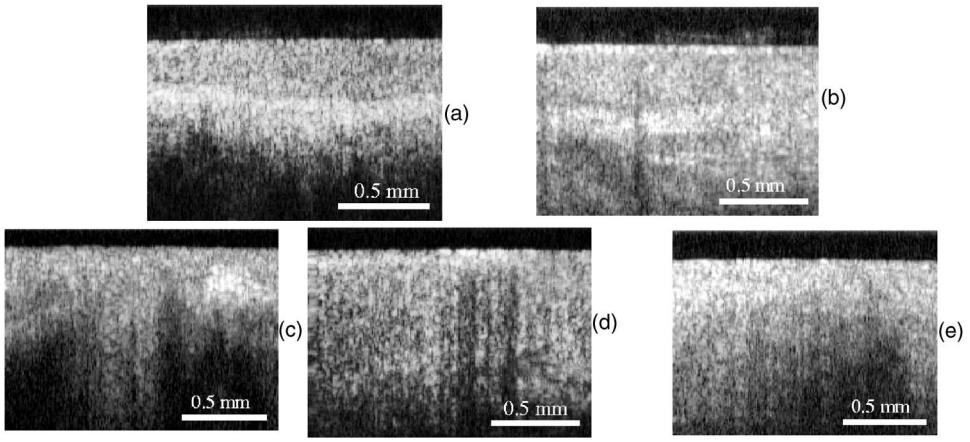

Fig. 1 OCT images of (a) healthy cervix, (b) dysplasia 1 and 2, (c) cervical metaplasia, (d) cervical leukoplakia, and (e) cervical neoplasia. OCT images (a) and (b) can be easily differentiated visually from (c), (d), and (e), but groups of images (a) (b), and (c), (d), and (e) have the same structure, and additional processing can help to distinguish these pathologies.

eters to describe the scattering medium: the total scattering coefficient and the backscattering coefficient,[14,15] or the total scattering coefficient and mean cosine of the scattering angle.[16] In this work, a reconstruction algorithm is proposed that allows one to estimate three scattering parameters, namely, the total scattering coefficient, the backscattering probability, and the variance of the small-angle scattering phase function. All three parameters influence essentially the shape of the OCT signal in a multiple scattering medium. The proposed model of OCT signal[17] is based on the wave theory of light propagation in the scattering medium. It accounts for the effects of coherent backscattering, which cannot be described in the frame of the theory of radiation transport. Nevertheless, it allows for calculation of an OCT image using the solution of radiative transfer equation (RTE) under the small-angle approximation[18] or the refined small-angle diffuse approximation.[17] The first one is less restrictive in comparison with the second one (also known as the extended Huygens-Fresnel principle[19]), since it does not impose limitations on the angular width of the probing beam or on the probing depth. The described model is suitable for arbitrary stratification of scattering parameters of the medium; however, one has to limit the number of layers to obtain unique solution of the inverse problem. For a two-layered model of the scattering medium, eight parameters are to be reconstructed: the position of front boundary, total scattering coefficient, backscattering probability, and variance of small-angle scattering function in each layer. Using a genetic algorithm permits one to reduce the time for reconstruction of the target parameters significantly, compared to standard fitting procedures that work well with a smaller number of unknowns.

In this work, the results of testing the reconstruction algorithm on model media are demonstrated, and the accuracy of reconstruction of scattering parameters for different regimes of OCT signal decay is studied.[20] The algorithm was applied to estimate the scattering characteristics of two tissue layers by *in vivo* OCT images of uterine cervix in different states (healthy cervix, dysplasia, metaplasia, and leukoplakia) based on the data obtained at the M.D. Anderson Cancer Center (Texas) and at Nizhny Novgorod State Medical Academy (Russia). A possibility for differentiation of various pathologies of biological tissue by reconstructed scattering parameters is shown by an example of cervical leukoplakia and dysplasia 2 to 3.

2 Theoretical Model of the Optical Coherence Tomography Signal

As far as optical scattering is concerned, biological tissue contains a variety of scatterers with sizes smaller, comparable, and larger than the wavelength. In general, the scatterer size distribution is given by a complicated function.[21] The majority of soft biological tissues are characterized by strong forward scattering, where, in a single interaction, an average photon changes its direction by less than one tenth of a radian. Therefore, a correct description of the light propagation at large distances within the tissue should take into account the effects of multiple small-angle scattering. In this work, we apply a theoretical model of the OCT signal in a layered medium, which accounts for changes in the beam structure caused both by small-angle scattering at small depths and by light diffusion at large depths. Light distribution in the medium, which occupies semi-infinite space $z>0$, with predominant scattering along the z direction, is described in the frame of the stationary RTE in small-angle approximation:[18]

$$\left\{\frac{\partial}{\partial z}+\mathbf{n}_\perp\cdot\nabla_\perp+[\mu_s(z)+\mu_a(z)]\right\}L(z,\boldsymbol{\rho},\mathbf{n}_\perp)$$
$$=\frac{\mu_s(z)}{4\pi}\int_{4\pi}x(z,|\mathbf{n}'_\perp-\mathbf{n}_\perp|)L(z,\boldsymbol{\rho},\mathbf{n}'_\perp)d\mathbf{n}'_\perp. \qquad (1)$$

Here, L is the light radiance depending on transversal coordinate $\boldsymbol{\rho}$ and on transversal angular deviation $n_\perp$ (related to beam axis); μ_s, the total scattering coefficient of the medium; μ_a, the absorption coefficient; $x(z,\gamma)$, the scattering phase function; and $\gamma=|n'_\perp-n_\perp|$, the scattering angle. To allow for layered structure, the characteristics of the medium contain dependence on the longitudinal coordinate z. Although light is scattered mainly in the forward direction, we cannot neglect the backscattering, since it plays the main role in forming the OCT signal. However, the probability of backscattering is a

small parameter, which further justifies the use of the single backscattering approximation to calculate the OCT signal. According to the prior assumptions, in the first-order approximation the scattering phase function can be presented as a sum of a small-angle scattering phase function $x_1(z,\gamma)$ that tends to zero for $\gamma > \pi/2$, and a constant that corresponds to isotropic scattering:[17]

$$x(z,\gamma) = [1 - 2p_b(z)]x_1(z,\gamma) + 2p_b(z). \tag{2}$$

The small-angle scattering function $x_1(z,\gamma)$ obeys the normalization requirement:

$$\frac{1}{2}\int_0^\infty x_1(z,\gamma)\gamma d\gamma = 1. \tag{3}$$

Backscattering probability p_b is determined by the part of the light energy scattered into the backward hemisphere:

$$p_b(z) = \frac{1}{2}\int_{\pi/2}^{\pi} x(z,\gamma)\sin\gamma d\gamma. \tag{4}$$

Equation (1) has an analytically derived spectrum over transversal coordinate

$$\tilde{U}^{\mathrm{UPS}}(z,\mathbf{h}) = \frac{1}{4\pi^2}\int_{-\infty}^{\infty} U^{\mathrm{UPS}}(z,\boldsymbol{\rho})\exp(-i\mathrm{h}\rho)d\boldsymbol{\rho},$$

for the intensity distribution from the unidirectional point source (UPS),

$$U^{\mathrm{UPS}}(z,\boldsymbol{\rho}) = \int_{4\pi} L(z,\boldsymbol{\rho},\mathbf{n}_\perp)d\mathbf{n}_\perp,\mathbf{h},$$

spatial frequency. For a plain-layered medium:[17]

$$\tilde{U}^{\mathrm{UPS}}(z,\mathbf{h}) = \frac{1}{4\pi^2}\exp\left\{-\int_0^z [\mu_s(z') + \mu_a(z')]dz' + \int_0^z \mu_s(z')[1 - 2p_b(z')]\tilde{x}_1[z', h(z-z')]dz'\right\}. \tag{5}$$

Here, $h=|h|$, $\tilde{x}_1(z,p)$ is the angular spectrum for small-angle scattering phase function $x_1(z,\gamma)$ (J_0 is the zero-order Bessel function),

$$\tilde{x}_1(z,p) = \frac{1}{2}\int_0^\infty x_1(z,\gamma)J_0(p\gamma)\gamma d\gamma. \tag{6}$$

The second integral in the exponent of Eq. (5) represents energy transfer from the nonscattered component of UPS intensity,

$$U_0^{\mathrm{UPS}}(z,\boldsymbol{\rho}) = \delta(\boldsymbol{\rho})\exp\left\{-\int_0^z [\mu_s(z') + \mu_a(z')]dz'\right\},$$

into diffuse components due to multiple small-angle scattering [$\delta(\boldsymbol{\rho})$ is a 2-D Dirac delta function].

In the case of a distributed source with intensity at depth z in the absence of scattering given by the function $A(z,\rho)$, the intensity distribution in the scattering medium can be calculated as the convolution over transverse coordinate,

$$U(z,\boldsymbol{\rho}) = \int_{-\infty}^{\infty} A(z,\boldsymbol{\rho}')U^{\mathrm{UPS}}(z,\boldsymbol{\rho}-\boldsymbol{\rho}')d\boldsymbol{\rho}', \tag{7}$$

and the intensity distribution for ballistic component as,

$$U_0(z,\boldsymbol{\rho}) = A(\boldsymbol{\rho})\exp\left\{-\int_0^z [\mu_s(z') + \mu_a(z')]dz'\right\}. \tag{8}$$

With the assumption of strong anisotropy of the scattering function, the OCT signal from the depth z^* is formed by single backscattering of photons at the depth z^*, and the amount of backscattered light is defined by the product $x(z^*,\pi)\mu_s(z^*)U(z^*,\boldsymbol{\rho})$. Backscattered photons then travel to the receiving plane $z=0$, undergoing mostly small-angle scattering and covering the same longitudinal distance z^*.

The OCT signal is represented by the current at the square-law heterodyne detector and considered as a squared AC signal from interferometer $I=\langle i^2\rangle$. As a simplification, the low-coherent light source is assumed to be delta-correlated so that the imaging depth inside the medium is in unequivocal correspondence with the length of the reference arm. If one assumes the propagated light to be statistically independent from the backscattered light, the OCT signal $I(z^*)$ can be written as the surface integral[13,17]

$$I(z^*) = x(z^*,\pi)\mu_s(z^*)B\int_{-\infty}^{\infty} U^2(z^*,\boldsymbol{\rho})d\boldsymbol{\rho} = 2p_b(z^*)\mu_s(z^*)B\int_{-\infty}^{\infty} U^2(z^*,\boldsymbol{\rho})d\boldsymbol{\rho}, \tag{9}$$

where B is a constant for a specific OCT device. However, another approach accounting for correlations between the light that propagates forward and backward requires more accurate procedure of statistical averaging squared intensity $\langle U^2\rangle$,[13] and eventually yields some different expression for the OCT signal:

$$I(z^*) = 2p_b(z^*)\mu_s(z^*)B\int_{-\infty}^{\infty} [2U^2(z^*,\boldsymbol{\rho}) - U_0^2(z^*,\boldsymbol{\rho})]d\boldsymbol{\rho}. \tag{10}$$

For further analysis, we consider the probing beam in the absence of scattering to be focused into a spot size a_0 at distance f from the boundary of the medium (Fig. 2). The resulting undisturbed intensity has a Gaussian distribution:

$$A(z,\boldsymbol{\rho}) = \frac{P_s\exp[-\rho^2/a^2(z)]}{\pi a^2(z)}, \tag{11}$$

where

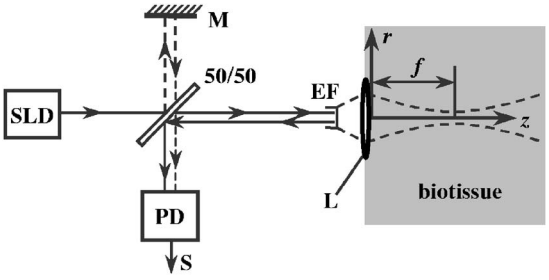

Fig. 2 A principal scheme of OCT setup. SLD (superluminescent diode), M (reference mirror), EF (end of optical fiber), L (lens), PD (photodetector), S (OCT signal), and f (focusing depth).

$$a^2(z) = a_0^2 + \left[\frac{(z-f)\lambda}{2\pi n a_0}\right]^2,$$

λ is the central wavelength, n is the mean refractive index of the medium, and P_S is the power of the probing beam. Following Eqs. (5) and (7)–(11), one obtains the normalized expression for the OCT signal $I(z)$, depending on the probing depth z,

$$I(z) = Bp_b(z)\mu_s(z)\exp\left\{-2\int_0^z [\mu_s(z') + \mu_a(z')]dz'\right\} \times\left(\int_0^\infty \exp\left\{-\frac{a^2(z)h^2}{2} + 2\int_0^z \mu_s(z')[1 - 2p_b(z')]\tilde{x}_1[z', h(z-z')]dz'\right\} hdh - \frac{1}{2a^2(z)}\right). \quad (12)$$

Equation (12) is valid for arbitrary stratification of scattering characteristics of the medium along the coordinate z. In the case of a two-layered structure, integration over depth in both square brackets can be performed analytically by proper choice of a model for small-angle scattering function $x_1(\gamma)$. In our simulation, the small-angle scattering function is taken in a Gaussian shape[19] with single parameter $\langle\gamma^2\rangle$ which, according to the requirement in Eq. (3), characterizes both width and peak value of the function $x_1(z,\gamma)$:

$$x_1(z,\gamma) = \frac{4}{\langle\gamma^2(z)\rangle}\exp\left[-\frac{\gamma^2}{\langle\gamma^2(z)\rangle}\right]. \quad (13)$$

The employed expression for $x_1(z,\gamma)$ possesses a simple analytical angular spectrum:

$$\tilde{x}_1(z,p) = \exp\left[-\frac{\langle\gamma^2(z)\rangle p^2}{4}\right]. \quad (14)$$

According to Eq. (2), the total scattering phase function is presented as the sum of a Gaussian-shaped small-angle part and a constant, which represents isotropic scattering and, particularly, backscattering:

$$x(z,\gamma) = \frac{4[1-2p_b(z)]}{\langle\gamma^2(z)\rangle}\exp\left[-\frac{\gamma^2}{\langle\gamma^2(z)\rangle}\right] + 2p_b(z). \quad (15)$$

The model in Eq. (15) was verified by its comparison to the scattering phase function calculated for spherical scattering particles using Mie formulas. The parameters p_b and $\langle\gamma^2\rangle$ were defined by the calculated scattering phase function $x_{Mie}(\gamma)$:

$$p_b = \frac{x_{\mathrm{Mie}}(\pi)}{2}, \quad \langle\gamma^2\rangle = \frac{1}{2\cdot(1-2p_b)}\int_0^\infty \gamma^3[x_{\mathrm{Mie}}(\gamma) - 2p_b]d\gamma. \quad (16)$$

Figure 3 demonstrates good agreement between the Mie scattering phase function for two model media and the scattering function in Eq. (15) with the parameters calculated according to Eq. (16).

3 Algorithm for Reconstruction of Tissue Scattering Properties

In the proposed algorithm, the scattering medium is assumed to be plane layered with N layers with different optical properties. Each i'th layer is characterized by the total scattering coefficient $\mu_{s,i}$, the backscattering probability $p_{b,i}$, the variance of a small-angle scattering function $\langle\gamma_i^2\rangle$, and the position of the layer front boundary l_i. These parameters are recovered via fitting of the experimental OCT signal versus depth $I_e(z)$ by the theoretical curve $I_t(z,\vec{v})$, where

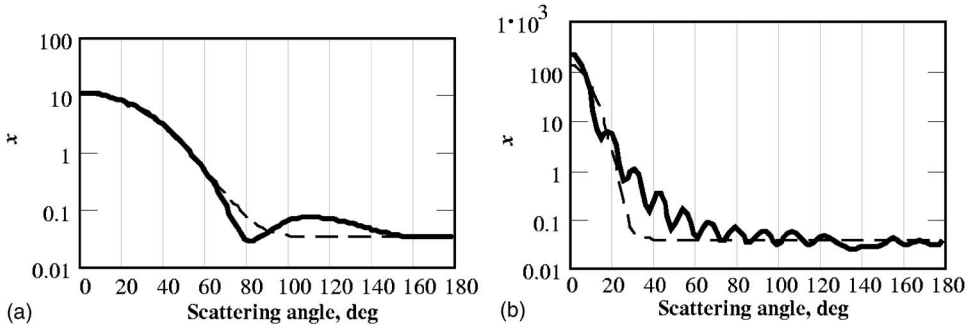

Fig. 3 Verification of the model for scattering phase function x. Solid line: Mie scattering phase function; dashed line: scattering phase function calculated according to Eq. (15). (a) Monodisperse medium with the size of scattering particles comparable to the wavelength. (b) Two-component medium containing scatterers with size much larger as well as much smaller than the wavelength.

$$\vec{v} = (\vec{l}, \vec{\mu}_s, \vec{p}_b, \langle \vec{\gamma}^2 \rangle),$$

$$\vec{l} = (l_1, \ldots, l_N),$$

$$\vec{\mu}_s = (\mu_{s,1}, \ldots, \mu_{s,N}),$$

$$\vec{p}_b = (p_{b,1}, \ldots, p_{b,N}),$$

$$\langle \vec{\gamma}^2 \rangle = (\langle \gamma_1^2 \rangle, \ldots, \langle \gamma_N^2 \rangle).$$

The experimental OCT curve $I_e(z)$ can be a single A-scan as well as a series of neighboring A-scans averaged over the transverse coordinate. The latter approach allows us to reduce noise variance. The theoretical OCT signal $I_t(z,\vec{v})$ is calculated using Eq. (12) for each point $\vec{v}$ in the space of parameters. A mean-square deviation of the logarithms of the experimental and fitting theoretical curves yields the discrepancy for the varying set of tissue parameters. In this case, the "true" medium parameters are obtained as a result of minimizing the integral within the given range of values,

$$\vec{v} = \arg\min_{\vec{v}} \int_0^Z \log^2[I_t(z,\vec{v})/I_e(z)]dz, \qquad (17)$$

or

$$\vec{v} = \arg\min_{\vec{v}} \int_0^Z \log^2\{[I_t(z,\vec{v})/I_t(0,\vec{v})]/I_e(z)\}dz, \qquad (18)$$

where Z is the maximum depth of the OCT signal. The discrepancy in Eq. (17) is used if the absolute value of the OCT signal [constant B in Eq. (12)] is known. This value can be measured directly before the OCT imaging procedure, using, for example, a calibration medium. If the information about the absolute value of the OCT signal is not available, we use discrepancy in Eq. (18). In this case, the reconstruction of the scattering parameters is less accurate (see Sec. 5).

Finding the global minimum of Eq. (17) or (18) with I_t defined by Eq. (12) is time consuming and computationally intensive. We applied the genetic algorithm[22] to minimize the integrals of Eq. (17) or (18), which reduced computational time in comparison with conventional fitting methods. Reconstruction of tissue parameters using the theoretical model described in Sec. 2 takes less than a minute on a Pentium IV 1.8 GHz for each OCT experimental curve, which has 100 pixels in the z direction. The calculation was performed for the following input parameters of the genetic algorithm: the population size, 150; the number of iterations of the whole population, 100. For a two-layered model, the population size was increased up to 300 and the number of iterations up to 200. The reconstruction time in this case was about 1.5 min.

Figures 4–6 demonstrate the results of the fitting procedure for OCT images of single-layered model medium and *in vivo* OCT images of cervix (Fig. 5 represents the two-layered model, Fig. 6, the single-layered model). The experimental OCT curve was obtained by transverse averaging the signal within the certain region of the tomogram, where the parameters of the medium are to be estimated, to reduce the noise variance. Both the noise variance in the experimental curve I_e and the covariance of the recovered tissue parameters decrease as the width of the window increases. Nevertheless, the medium should be relatively plane layered within the selected window.

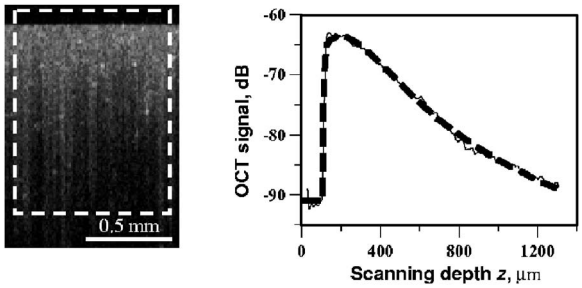

Scattering parameters	μ_s, 1/cm	p_b	$\langle\gamma^2\rangle$
Reconstructed	75±5	0.02±0.002	0.028±0.003
Predicted (Mie formula)	72	0.018	0.04

Fig. 4 Algorithm testing on model scattering medium of spherical polystyrene beads in glycerol. Concentrations of scatterers in solution: $C1 = 1.1 \times 10^5$ mm^{-3} (4.75-μm beads) and $C2 = 1.1 \times 10^{10}$ mm^{-3} (0.14-μm beads). OCT signal averaged over the selected window (thin solid line) is fitted with the theoretical curve (dashed line).

4 Algorithm Testing on Model Media

To test the algorithm, we conducted a series of experiments with model media. To create the model scattering medium, we used three types of spherical polystyrene beads with mean diameters of 0.14, 1, and 4.75 μm. The beads, taken at different concentrations, were dissolved in two different liquids, water and glycerol. Scattering phase functions and total scattering coefficients were calculated using Mie formulas and additionally measured using conventional methods.

For model experiments, we used an OCT setup designed at the Institute of Applied Physics (Russia) with a wavelength of 1.3 μm, both axial and transversal resolution equal to 15 μm, focusing depth of 500 μm, beam waist radius of 7.5 μm, scanning depth of 1 to 2 mm, and acquisition time for a 2-D image (200×200 pixels) of 1.5 sec.

An example of good agreement between predicted and reconstructed scattering parameters of a model medium is shown in Fig. 4. A model medium was a mixture of two types of polystyrene beads, one large, and the other small in comparison with the wavelength (4.75 and 0.14 μm). The front lobe and the rear part of the scattering phase function for the given medium are in good correspondence with Eq. (15), where the parameters p_b and $\langle \gamma^2 \rangle$ were defined from Eq. (16).

It is clearly seen from Fig. 4 that the theoretical dependence describes well the main features of the experimental OCT signal. According to the theoretical model, the fast decrease of the OCT signal at small probing depth is caused by multiple small-angle scattering. At larger depths, the regular beam structure collapses due to diffusion and backscattering, which, in fact, is weaker than small-angle scattering, and the

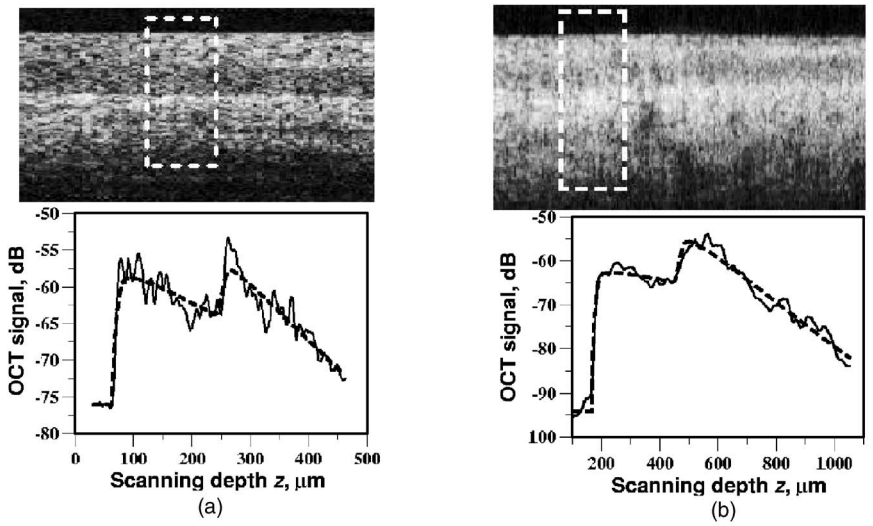

Layer	μ_s, 1/cm	p_b	$\langle\gamma^2\rangle$
1	50±4	0.07±0.01	0.4±0.2
2	100±10	0.2±0.03	0.1±0.04

Layer	μ_s, 1/cm	p_b	$\langle\gamma^2\rangle$
1	17±9	0.043±0.02	0.17±0.2
2	61±9	0.14±0.04	0.12±0.2

Fig. 5 OCT images and reconstructed parameters of normal uterine cervix. The two-layered model of OCT signal is used: first layer, epithelium; second layer stroma. Origin: (a) M.D. Anderson Cancer Center, and (b) Semashko Regional Hospital.

rate of OCT signal attenuation slows down. Both regions of fast and slow attenuation are observed in the experimental OCT images.

5 Possibility of Reconstruction Scattering Parameters of a Single Layer

While testing the reconstruction algorithm on model media with different concentration of scatterers, it was observed that in a number of cases the algorithm fails to reconstruct some of scattering parameters, which means that the inaccuracy of the estimated parameter is comparable to the value of the parameter itself. It was found that the number of well-reconstructed parameters depends on the shape of the OCT signal. The two specific regimes of OCT signal decay can be distinguished by a value of dimensionless optical width of the probing beam:

$$D = \frac{3\mu_s a}{\sqrt{\langle\gamma^2\rangle}}. \tag{19}$$

This parameter defines the relation of the beam radius to the average transversal deflection of a photon at a single scattering event. In the case of $D \ll 1$, the probing beam is considered to be optically narrow, since at a single scattering the photons leave the main body of the beam. This effect causes Beer's law attenuation of the probing beam at small depths, and the OCT signal shows exponential dependence versus depth:

$$I(z) \propto \exp(-2\mu_s z). \tag{20}$$

At larger depths, when major part of the light energy is transformed into scattered components, diffusion regime of OCT signal attenuation is observed:

$$I(z) \propto \frac{\exp(-4p_b\mu_s z)}{\mu_s\langle\gamma^2\rangle z^3}, \quad \mu_a \ll 2p_b\mu_s. \tag{21}$$

The transition point between these areas is located at the depth τ^* and can be estimated from the transcendent equation,

$$\ln(\tau^*) - 2\tau^*(1-2p_b) = 2\ln(D/\sqrt{3}). \tag{22}$$

For an optically wide beam ($D > 1$), scattered photons stay within the main body of the beam after several scattering events; therefore, OCT signal decay does not have a fast exponential region. Figure 7 demonstrates OCT signal decay for both regimes: an optically narrow beam $D \ll 1$ and an optically wide probing beam $D \geqslant 1$.

According to Eqs. (20)–(22), the behavior of the OCT signal for an optically narrow beam in the whole range of probing depths is defined by three scattering parameters: the total scattering coefficient μ_s describes the rate of fast exponential attenuation, the variance $\langle\gamma^2\rangle$ influences the location of the transition point, and the product $p_b\mu_s$ gives the absolute value of the OCT signal. Thus, using the rapidly decaying part of OCT signal in the case of an optically narrow beam, one can reconstruct the value of μ_s and, if the absolute value of the OCT signal is known, the value of p_b. By the diffusive part of

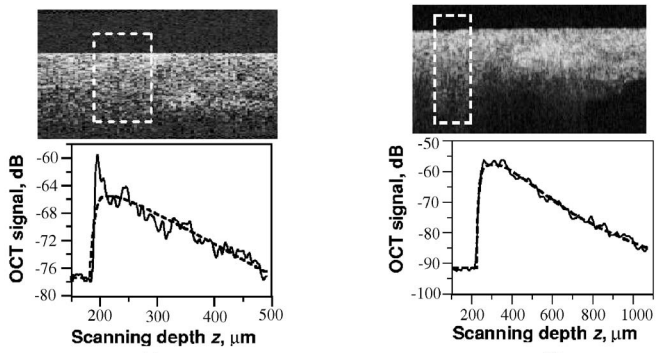

μ_s, 1/cm	p_b	$\langle\gamma^2\rangle$
58±2	0.013±0.001	0.4±0.1

μ_s, 1/cm	p_b	$\langle\gamma^2\rangle$
91±10	0.02±0.003	0.026±0.005

Fig. 6 OCT images and reconstructed parameters of cervical metaplasia. A single-layered model of OCT signal is used. Origin: (a) M.D. Anderson Cancer Center, and (b) Semashko Regional Hospital.

the OCT signal, it is possible to reconstruct the $\langle\gamma^2\rangle$ value as well. However, the depth at which a useful signal can be acquired using a conventional OCT system is limited by the signal-to-noise ratio or by scanning depth, and the diffusive region may not be observed in the OCT signal.

The attenuation behavior of an optically wide probing beam (Fig. 7, right) is mostly diffusive, and the rate of decay is defined by the combinations of parameters $p_b\mu_s$ and $\langle\gamma^2\rangle\mu_s$. These two combinations of parameters can be reconstructed with better accuracy in comparison with separate reconstruction of μ_s, p_b, and $\langle\gamma^2\rangle$.

Figures 8–10 show the confidence areas of reconstructed parameters (see confidence area estimation procedure in Appendix A in Sec. 8.). Larger areas correspond to lesser accuracy of the estimated parameter. Different level curves show confidence areas for different noise variance $\sigma^2=0.1$, 1, and 4.

For an optically narrow probing beam, the value of μ_s can be reconstructed with high accuracy (Figs. 9 and 10), and in the case when the absolute value of the OCT signal is known (Fig. 9), $p_b\mu_s$ can also be reconstructed, since the OCT signal from the medium surface is proportional to the backscattering coefficient in Eq. (12). For an optically wide probing beam (Fig. 10)—the typical situation for endoscopic OCT—products p_b, μ_s, and $\langle\gamma^2\rangle\mu_s$ can be reconstructed better than μ_s, p_b, and $\langle\gamma^2\rangle$ separately.

6 Reconstruction of Scattering Parameters of Uterine Cervix Layers by *In Vivo* Optical Coherence Tomography Images

Figures 5 and 6 demonstrate examples of fitting the experimental OCT signal by theoretical OCT curves and estimating scattering parameters of the normal uterine cervix and cervical metaplasia. The OCT images were obtained at the M.D. Anderson Cancer Center (Texas) and Semashko Regional Hospital (Nizhny Novgorod, Russia). The OCT device used at the M.D. Anderson Cancer Center had the following technical

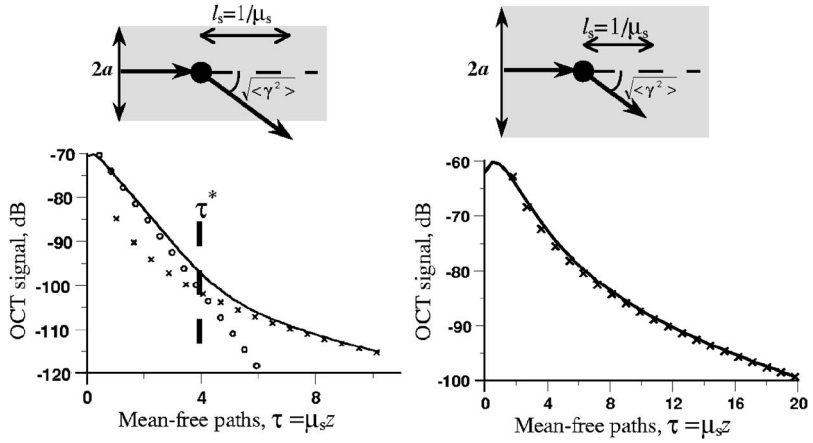

Fig. 7 Attenuation rate of the OCT signal versus depth in cases of an optically narrow beam $D=0.25$ (left) and an optically wide beam $D=3$ (right). OCT signals calculated by Eq. (12) are shown by solid lines, fast exponential attenuation of the OCT signal (20), by ○ signs, and diffusion regime of OCT signal attenuation [Eq. (21)], by × signs. In the left plot, τ^* shows the transition point between the two OCT signal attenuation regimes.

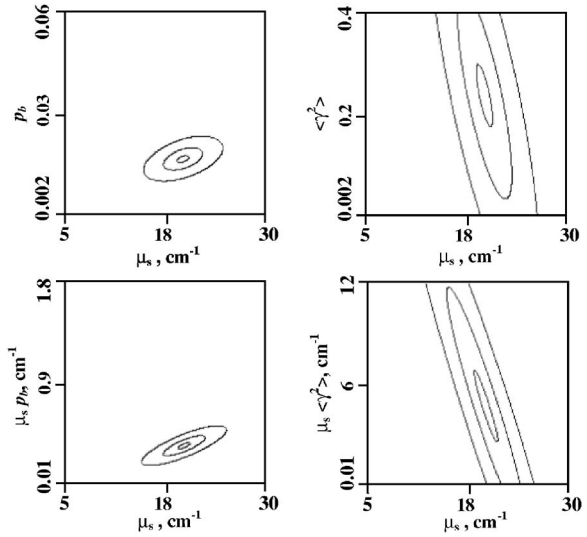

Fig. 8 Confidence areas of estimated scattering parameters in the case of an optically narrow beam $D=0.25$. Absolute value of the OCT signal is known and the discrepancy in Eq. (17) is applied for the reconstruction procedure. The scattering medium is a water solution of spherical polystyrene beads of 1 μm in diameter with concentration $C=0.44\times10^5$ mm^{-3}. True scattering parameters of the medium are $\mu_s=20$ 1/cm, $\langle\gamma^2\rangle=0.23$, and $p_b=0.017$. Well-defined parameters are μ_s and $\mu_s p_b$.

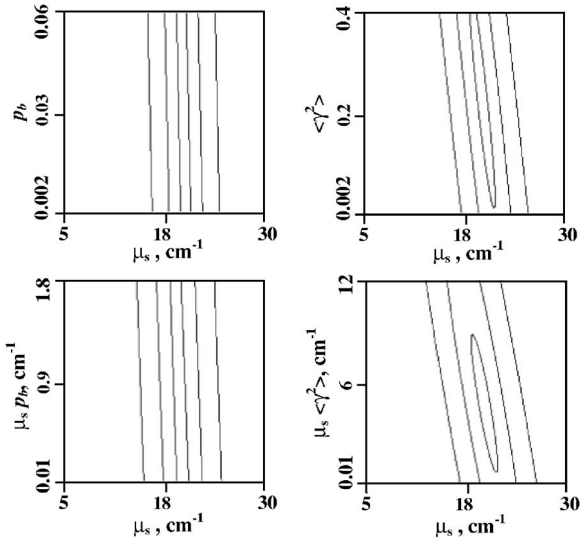

Fig. 9 Confidence areas of estimated scattering parameters in the case of an optically narrow beam $D=0.25$. Absolute value of the OCT signal is unknown and the discrepancy in Eq. (18) is applied for the reconstruction procedure. The scattering medium is a water solution of spherical polystyrene beads of 1 μm in diameter with concentration $C=0.44\times10^5$ mm^{-3}. True scattering parameters of the medium are $\mu_s=20$ 1/cm, $\langle\gamma^2\rangle=0.23$, and $p_b=0.017$. Well-defined parameter is μ_s.

characteristics: 800-nm light source, 15-μm coherence length, 500-μm focusing depth from the tissue surface, 7.5-μm beam waist radius, and the size of the OCT image 100×1496 pixels. The OCT device used at Semashko Regional Hospital had the same technical characteristics as the one employed in the model experiments described in Sec. 4.

For reconstruction, Eq. (17) for OCT signal discrepancy was used, since the absolute value of the OCT signal was measured before the imaging procedure using calibration media. For healthy cervix due to its layered structure (epithelium and stroma), a two-layered theoretical model was applied in the algorithm (Fig. 5). The jump in the OCT signal is caused by the differences of backscattering coefficients $p_b\mu_s$ between the first and the second layer. In Fig. 6, OCT images and reconstructed parameters of cervical metaplasia are shown (a single-layered theoretical model was employed).

The results of reconstruction scattering parameters of leukoplakia and neoplastic areas in multiple images from a single patient with cervical precancer are given in Fig. 11. The examples of OCT images of these pathologies are shown in Figs. 1(d) and 1(e). In the reconstruction algorithm, the single-layered model of the OCT signal is used for both leukoplakia and neoplastic areas. In the realized case of an optically narrow beam, both parameters μ_s and p_b can be estimated with the relative errors 10 and 20%, correspondingly, and $\langle\gamma^2\rangle$ cannot be determined well (see Figs. 8 and 9 explaining the large discrepancy of determination $\langle\gamma^2\rangle$ value in the case of an optically narrow beam). For all processed images, the estimated scattering parameters of leukoplakia and neoplastic tissue are localized in two separate nonoverlapping regions on the plane of scattering parameter. The boundary between these regions is marked with the dashed line (Fig. 11). This separation can provide a basis for identification of abnormal changes in the tissue structure. As seen from Fig. 11, the parameter μ_s can serve as a criterion for distinguishing leukoplakia and dysplasia 2 to 3. The values of p_b are similar in both leukoplakia and dysplasia 2 to 3, therefore, the backscattering probability cannot serve as a representative parameter.

Figure 12 demonstrates changes of reconstructed scattering parameters of tissue layers when moving from healthy cervix to carcinoma focus. It is clearly seen from the figure that both total scattering and backscattering coefficients increase in the epithelium and decrease in stroma. The two-layered model of OCT signal was used for structured images [Figs. 12(a)–12(c)], and a single-layered model, for unstructured images [Fig. 12(d)]. It is seen from the figure that on the boundary of structured and unstructured images, the backscattering coefficients of epithelium and stroma become equal. These data can be used to identify the stage of the neoplasia process after appropriate verification at different patients.

The results of processing of the obtained data show that the estimated values of the total scattering coefficient are in a good agreement with the reported data for these types of tissue.[23,24]

7 Discussion

The described algorithm can aid visual analysis of OCT images by providing an additional tool for quantitative assessment of biological tissue optical properties and, thus, improving the capabilities of OCT in identification of pathological processes. Since a 1-D model of the OCT signal is employed in the algorithm, the processed region of a tomogram must be stratified. The speckle noise of the average OCT signal and the covariance of estimated parameters can be reduced signifi-

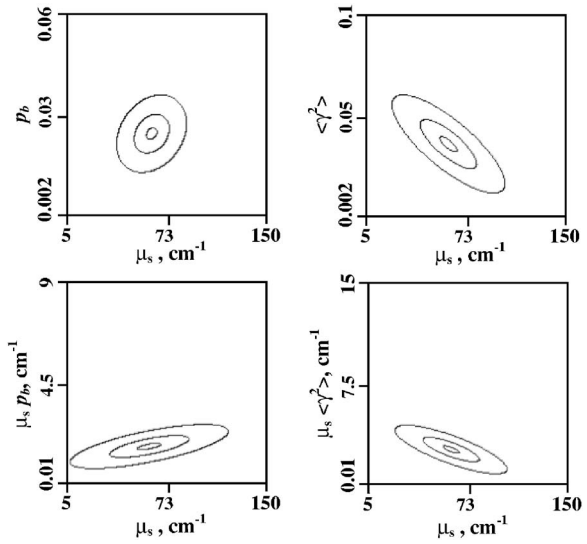

Fig. 10 Confidence areas of estimated scattering parameters in the case of an optically wide beam $D=2.16$. The absolute value of the OCT signal is known and the discrepancy in Eq. (17) is applied for the reconstruction procedure. The scattering medium is a glycerol solution of spherical polystyrene beads of 4.75 μm in diameter with concentration $C=1.1\times10^5$ mm^{-3} and 0.14-μm beads with concentration $C=1.1\times10^{10}$ mm^{-3}. True scattering parameters of the medium are $\mu_s=72$ 1/cm, $\langle\gamma^2\rangle=0.04$, and $p_b=0.018$. Well-defined parameters are $\langle\gamma^2\rangle\mu_s$ and $p_b\mu_s$.

cantly by choosing a wider region of an OCT image for averaging out. The accuracy of the reconstruction procedure of scattering parameters in multilayered medium decays with the decrease of thickness of a single layer. Tomograms of mucosae of the uterine cervix, larynx, esophagus, etc., are the most appropriate for processing, because the architecture of these types of biological tissue is close to plane layered, the layers are quite thick, and can be visualized on an OCT image. The reconstruction procedure allows for estimation of parameters of multilayered media with three or more numbers of layers (i.e., retina) on condition that some additional information about relative variation of parameters from layer to layer is available. In the general case of multilayered media, separate reconstruction of all three parameters (μ_s, p_b, and $\langle\gamma^2\rangle$) in each layer cannot be realized. To apply the proposed algorithm in medical practice, it is necessary to collect statistically sufficient OCT data, which should satisfy the following requirements. 1. The imaging procedure should be performed with calibrated OCT devices. Calibration can be realized using test scattering medium with well-defined optical properties. 2. The OCT data should be histologically proved, and reliability of these data strongly depends on the exact coincidence of OCT and biopsy sites. 3. The quantity of OCT images should be large enough to reflect all variations of scattering parameters in real biological tissue caused by changes of optical properties inside one patient and by patient-to-patient changes. If the latter variations are large, so that the confidence areas corresponding to different tissue states overlap, the reconstruction algorithm can only be employed for comparison of different tissue areas inside one patient (see examples of alteration of the tissue properties compared to the two pathological states in Fig. 11, and healthy tissue to neoplasia in Fig. 12).

The theoretical approach used in the numerical algorithm is based on RTE solution under small-angle approximation and was approved by reconstructing optical properties of model media. The accuracy of this approach is sufficient for evaluating the detailed structure of the scattered beam at small as well as at large imaging depths, since the applied approximation reflects angular distribution of light in relation with the actual shape of small-angle scattering phase function. On the contrary, previously reported theoretical models[14,19] account mostly for average characteristics of the scattering phase function, but not the shape.

While processing the image, we estimate parameters averaged over the spectral band. For realizing OCT, broadband spectra are required and one should account for dependence of scattering characteristics on the wavelength. For the OCT setup used in our experiments, spectral width was 40 nm. For the given band ($<5\%$), the scattering parameters (μ_s, p_b, and $\langle\gamma^2\rangle$) vary within the 4 to 7% range, which was verified for model media using Mie formulae. The variance due to wavelength dispersion is less than the inaccuracy of the reconstruction procedure (see the table in Fig. 4). In the case of an

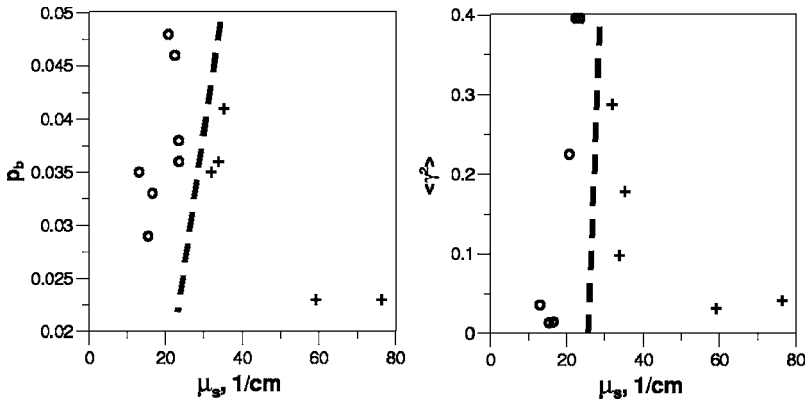

Fig. 11 Result of processing 13 OCT images obtained from a patient with cervical dysplasia 2 to 3 and neighboring leukoplakia (one clinical example). Points on the plane correspond to estimated scattering parameters of biological tissue: + is dysplasia 2 to 3 and O is leukoplakia. The dashed line separates scattering parameters corresponding to different types of pathology. Estimated relative errors of μ_s, p_b, and $\langle\gamma^2\rangle$ are 10, 20, and 70%, correspondingly.

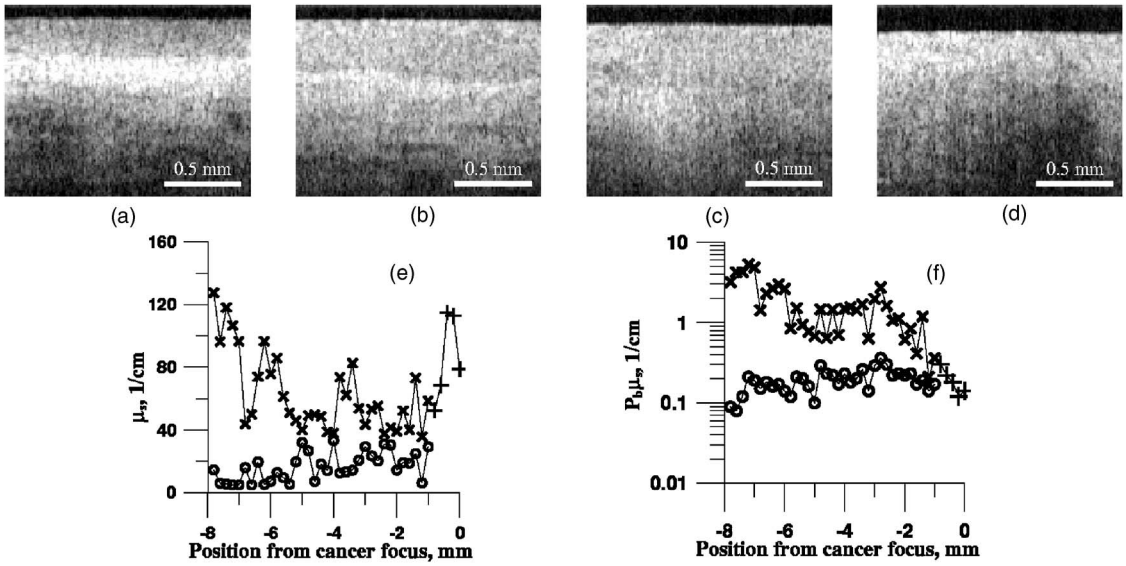

Fig. 12 Result of processing of 19 OCT images obtained from a patient with cervical neoplasia (one clinical example). One to three windows for averaging were chosen for calculation of scattering parameters from each OCT image. OCT images (a) and (d) demonstrate alterations in biological tissue structure from (a) healthy to (d) carcinoma (a) 5 mm from the visual tumor border (7 mm from the visual tumor focus), (b) 2 mm from the visual tumor border (4 mm from the visual tumor focus), (c) the visual tumor border, and (d) the visual tumor focus. Plots (e) and (f) show changes in reconstructed scattering parameters (total scattering coefficient μ_s and backscattering coefficient $\mu_s p_b$) for ○ epithelium and × stroma in dependence on the distance from carcinoma focus. Near (d) the carcinoma focus, the OCT images look unstructured, and a single-layered model of tissue is used. Estimated relative errors of μ_s and $\mu_s p_b$ for epithelium are 30 and 8%, and for stroma are 20 and 20%, correspondingly.

ultrabroadband source (150 to 300 nm), variation of scattering parameters may be much stronger, and the reconstruction algorithm should be refined by convolving the theoretical model in Eq. (12) with the source spectrum.

Acknowledgments

This work was partly supported by the Russian Foundation for Basic Research (grant numbers 01-02-17721, 03-02-06420, and 04-02-17108), and the United States Civilian Research and Development Foundation (CRDF Award Number RB2-2389-NN-02). The authors are grateful to Nizhny Novgorod State Medical Academy and Regional Hospital for assistance in clinical investigations. Special thanks to Michele Follen (M.D. Anderson Cancer Center) and Andres Zuluaga (InfraReDx, Incorporated) for provided OCT images and histological data.

Appendix A: Estimation of Covariance and Confidence Regions of Reconstructed Parameters

To estimate covariance and confidence regions for reconstructing scattering parameters, we applied Cramer-Rao low bound[25]

$$E\{(\vec{v}-\vec{v}_0)(\vec{v}-\vec{v}_0)^T\} \geq \hat{\mathbf{F}}^{-1}, \tag{23}$$

where the Fisher matrix is $\hat{\mathbf{F}}$, expectation $E\{\cdot\}$, vector of scattering parameters, defined in Sec. 3, is $\vec{v}$, and the vector of "true" scattering parameters is $\vec{v}_0$. Under the consideration of the simplest case, when the logarithm of experimental OCT signal is the sum of logarithm of the theoretical OCT signal and additive noise ξ with variance σ^2

$$\log I_e(z_i,\vec{v}) = \log I_t(z_i,\vec{v}) + \xi_i, \tag{24}$$

the Fisher matrix can be written as follows,

$$F_{k,l} = \frac{1}{\sigma^2}\sum_{i=1}^{M} \frac{\partial \log I_t(z_i,\vec{v})}{\partial v_k}\frac{\partial \log I_t(z_i,\vec{v})}{\partial v_l}\bigg|_{\vec{v}=\vec{v}_0}. \tag{25}$$

Here, z_i is the coordinate z in the digitized OCT signal, M is the number of z_i points, and k,l are indices of vectors $\vec{v}$ and $\vec{v}_0$, corresponding to numbers of estimating parameters. Under the consideration of Eq. (24), the noise variance can be calculated as the mean-square deviation of theoretical OCT curve from the experimental one,

$$\sigma^2 = \frac{1}{M}\sum_{i=1}^{M} \log^2[I_t(z_i,\vec{v}_0)/I_e(z_i)]. \tag{26}$$

The matrix $\hat{\mathbf{F}}^{-1}$ can be calculated from Eqs. (25) and (26), and can be taken as the covariance matrix of estimating scattering parameters. This technique was used to estimate uncertainties of scattering parameters in Figs. 4–6, 11, and 12. Note that if the OCT signal absolute value is unknown and the discrepancy in Eq. (18) is applied for reconstruction procedure, one should use $I_t(z,\vec{v})/I_t(0,\vec{v})$ instead of $I_t(z,\vec{v})$ in Eqs. (24)–(26).

Confidence areas of estimated parameters for different noise variance σ^2 can be found using the Fisher matrix as well. Multidimensional probability density of estimated scattering parameters using Cramer-Rao low bound can be written as a function of vector $(\vec{v}-\vec{v}_0)$ and σ^2,

$$W(\vec{v}-\vec{v},\sigma)=\frac{1}{[(2\pi)^n \det(\hat{\mathbf{F}}^{-1})]^{1/2}} \times\exp\left[-\frac{1}{2}(\vec{v}-\vec{v}_0)^T\hat{\mathbf{F}}(\sigma)(\vec{v}-\vec{v}_0)\right], \quad (27)$$

where $(\cdot)^T$ is the operation of transposition. For the definite variance σ^2, the confidence area, confined within the level line $W(\vec{v}-\vec{v}_0,\sigma)=W_0$, can be found via the following equation,

$$\int_{W(\vec{v}-\vec{v}_0,\sigma)<W_0} W(\vec{v}-\vec{v}_0)d\vec{v}=0.5, \quad (28)$$

where 0.5 is the probability of location $\vec{v}$ in the confidence area.

References

1. J. M. Schmitt, "Optical coherence tomography (OCT): A review," *IEEE J. Sel. Top. Quantum Electron.* **5**(4), 1205–1215 (1999).
2. A. F. Fercher, W. Drexler, C. K. Hitzenberger, and T. Lasser, "Optical coherence tomography—principles and applications," *Rep. Prog. Phys.* **66**, 239–303 (2003).
3. A. M. Sergeev, V. M. Gelikonov, G. V. Gelikonov, F. I. Feldchtein, R. V. Kuranov, N. D. Gladkova, N. M. Shakhova, L. B. Snopova, A. V. Shakhov, I. A. Kuznetzova, A. N. Denisenko, V. V. Pochinko, P. Chumakov Yu, and O. S. Streltzova, "*In vivo* endoscopic OCT imaging of precancer and cancer states of human mucosa," *Opt. Express* **1**, 432–440 (1997).
4. F. I. Feldchtein, G. V. Gelikonov, V. M. Gelikonov, R. V. Kuranov, A. M. Sergeev, N. Gladkova, A. V. Shahkov, N. M. Shahkova, L. B. Snopova, A. B. Terent'eva, E. V. Zagainova, Yu. P. Chumakov, and I. A. Kuznetzova, "Endoscopic applications of optical coherence tomography," *Opt. Express* **3**(6), 257–269 (1998).
5. J. G. Fujimoto, C. Pitris, S. A. Boppart, and M. E. Brezinski, "Optical coherence tomo-graphy, an emerging technology for biomedical imaging and optical/biopsy," *Neoplasia* **2**, 9–25 (2000).
6. G. Zuccaro, N. D. Gladkova, J. Vargo, F. I. Feldchtein, J. Dumot, E. V. Zagaynova, D. Conwell, G. W. Falk, J. R. Goldblum, J. Ponsky, G. V. Gelikonov, and J. E. Richter, "Optical coherence tomography (OCT) in the diagnosis of Barrett's esophagus (BE), high grade dysplasia (HGD), intramucosal adenocarcinoma (ImAC) and invasive adenocarcinoma (InvAC)," *Gastrointest. Endosc.* **53**, 330 (2001).
7. N. M. Shakhova, V. M. Gelikonov, V. A. Kamensky, R. V. Kuranov, and I. V. Turchin, "Clinical aspects of the endoscopic optical coherence tomography and the ways for improving its diagnostic value," *Laser Phys.* **12**, 617–626 (2002).
8. P. F. Escobar, J. L. Belinson, A. White, N. M. Shakhova, F. I. Feldchtein, M. V. Kareta, and N. D. Gladkova, "Diagnostic efficacy of optical coherence tomography in the management of pre-invasive and invasive cancer of the uterine cervix and the vulva," *Int. J. Gyn. Cancer* **14**, 470–474 (2004).
9. G. V. Gelikonov, V. M. Gelikonov, S. U. Ksenofontov, A. N. Morosov, A. V. Myakov, Y. P. Potapov, V. V. Saposhnikova, E. A. Sergeeva, D. V. Shabanov, N. M. Shakhova, and E. V. Zagainova, "Compact optical coherence microscope," Chap. 20 in *Coherent-Domain Optical Methods. Biomedical Diagnostics, Environmental and Material Science*, V. V. Tuchin, Ed., pp. 345–362, Kluwer Academic Publishers, New York (2004).
10. R. Drezek, C. Brookner, I. Pavlova, I. Boiko, A. Malpica, R. Lotan, M. Follen, and R. Richards-Kortum, "Autofluorescence microscopy of fresh cervical tissue sections reveals alterations in tissue biochemistry with dysplasia," *Photochem. Photobiol.* **73**(6), 636–41 (2001).
11. T. Collier, A. Lacy, A. Malpica, M. Follen, and R. Richards-Kortum, "Near real time confocal microscopy of amelanotic tissue: Detection of dysplasia in *ex vivo* cervical tissue," *Acad. Radiol.* **9**, 504–512 (2002).
12. D. Arifler, M. Guillaud, A. Carraro, A. Malpica, M. Follen, and R. Richards-Kortum, "Light scattering from normal and dysplastic cervical cells at different epithelial depths: Finite difference time domain modeling with a perfectly matched layer boundary condition," *J. Biomed. Opt.* **8**(3), 484–494 (2003).
13. L. S. Dolin, F. I. Feldchtein, G. V. Gelikonov, V. M. Gelikonov, N. D. Gladkova, R. R. Iksanov, V. A. Kamensky, R. V. Kuranov, A. M. Sergeev, N. M. Shakhova, and I. V. Turchin, "Fundamentals of OCT and clinical applications of endoscopic OCT," Chap. 17 in *Coherent-Domain Optical Methods. Biomedical Diagnostics, Environmental and Material Science*, V. V. Tuchin, Ed., pp. 211–270, Kluwer Academic Publishers, New York (2004).
14. J. M. Schmitt and A. Knuttel, "Measurement of optical-properties of biological tissues by low-coherence reflectometry," *Appl. Opt.* **32**, 6032–6042 (1993).
15. I. V. Turchin, E. A. Sergeeva, L. S. Dolin, and V. A. Kamensky, "Estimation of biotissue scattering properties from OCT images using a small-angle approximation of transport theory," *Laser Phys.* **13**, 1524–1529 (2003).
16. P. E. Andersen, L. Thrane, H. T. Yura, A. Tycho, T. M. Jorgensen, and M. H. Frosz, "Advanced modelling of optical coherence tomography systems," *Phys. Med. Biol.* **49**(7), 1307–1327 (2004).
17. L. S. Dolin, "A theory of optical coherence tomography," *Radiophys. Quantum Electron.* **41**(10), 850–873 (1998).
18. A. Ishimaru, "Wave propagation and scattering in random media," v. 1, *Single Scattering and Transport Theory*, Academic Press, New York (1978).
19. L. Thrane and H. T. Yura, "Analysis of optical coherence tomography systems based on the extended Huygens-Fresnel principle," *J. Opt. Soc. Am. A Opt. Image Sci. Vis* **17**, 484–490 (2000).
20. I. V. Turchin, E. A. Sergeeva, N. M. Shakhova, and I. A. Kuznetsova, "OCT image processing algorithm for differentiation biological tissue pathologies," in *Biomedical Topical Meetings on CD-ROM, FH40*, The Optical Society of America, Washington, DC (2004).
21. J. M. Schmitt and G. Kumar, "Optical scattering properties of soft tissue: a discrete particle model," *Appl. Opt.* **37**, 2788–2797 (1998).
22. *Handbook of Genetic Algorithms*, L. Davis, Ed., Van Nostrand Reinhold, NY (1991).
23. *Tissue Optics: Light Scattering Methods and Instruments for Medical Diagnosis*, V. V. Tuchin, Ed., SPIE Press, Bellingham, WA (2000).
24. R. Hornung, T. H. Pham, and K. A. Keefe, "Quantitative near-infrared spectroscopy of cervical dysplasia *in vivo*," *Hum. Reprod.* **14**(11), 2908–2916 (1999).
25. H. L. Van Trees, *Detection, Estimation and Modulation Theory*, Wiley, New York (1991).